JOURNAL OF MATERIALS SCIENCE 24 (1989) 252-258

A new experimental technique for studying mass transport in liquid metals

I. Y. KHANDROS
IBM T. J. Watson Research Laboratory, Yorktown Heights, New York 10598, USA
M. OHRING
Department of Materials and Metallurgical Engineering, Stevens Institute of Technology, Hoboken, New Jersey 07030, USA

A new experimental technique was developed having general applicability to the study of a variety of mass transport effects in liquid metal alloys. This technique is based on the real-time monitoring of compositional changes at the outer diameter of a horizontally rotating bilayer melt tube through the use of isotope-excited X-ray fluorescence methods. The apparatus is described and applications to the measurement of interdiffusion coefficients as well as anomalous transport, involving the Rayleigh–Taylor instability, are discussed. Unlike prior methods for studying diffusion in liquid metals, the present technique eliminates uncertainties associated with solute redistribution during solidification. Another advantage is the ability to detect non-diffusive contributions to mass transport, in real time.

1. Introduction

Studies of diffusion and other transport phenomena in liquid alloys have been necessitated by the need to better understand transport mechanisms as well as by technological demands. The increased pressure on the precision of diffusion measurements in liquid alloys is due to the relative uniformity of diffusion coefficient values. In fact, the development of new theories is hampered by inconsistencies in experimental data which often overshadow the disagreement between the predictions of various models [1]. The work described in this paper represents an attempt to develop a new experimental technique for *in situ* measurements of diffusion coefficients in liquid alloys. A subsequent paper will present applications of the technique in the study of interdiffusion in a number of low-melting alloy systems.

Various methods to determine diffusion coefficients in liquid metals have been devised over the years and these have been discussed in the extensive review articles by Edwards *et al.* [2], Walls [3], Nachtrieb [4, 5] and Rigney [6], and in the recent book on the subject by Shimoji and Itami [7]. To briefly summarize, all three major techniques – capillary reservoir, long capillary, and shear cell – are plagued by experimental difficulties. Typical problems are entry losses, convection and solute accumulation at the capillary mouth [8] for the capillary–reservoir method and mixing during the initial contact of melts in the long capillary technique. Disturbances in the melt during shearing motions are a source of difficulty in the shear cell technique. Finally, the common weak point of almost all liquid metal diffusion measurements is the fact that the determinations of diffusion coefficients are based on "post-mortem" examinations of the solidified metal. This, despite the fact that the actual solute distribution in the liquid metal at the end of a diffusion cycle is strongly modified by mass transport and volume changes during solidification [9].

The new experimental technique described here involved the real-time monitoring of solute build-up during diffusion. The reason for employing an *in situ* measurement is twofold. First the problem of solute redistribution during solidification is eliminated. Secondly, interference from some other mode of mass transport can often be detected while directly observing kinetic changes. Anomalous transport effects can thus be inferred rather than making such a judgement later, based on an unusually high value of the resultant diffusivity, as is conventionally done. In essence, diffusivity values are extracted from the kinetics of concentration build-up rather than from the solute profile at the end of a diffusion anneal. The other distinct feature of the experimental method is the rotation of the two melt layers which comprise the diffusion couple. While the first layer of the couple rotates with a centrifugal acceleration of typically 100 *g* the second, less dense melt layer is poured. Until this second melt picks up high speed there is a large disparity in effective densities which minimizes convective mixing. By pouring on to the rapidly moving melt surface the second layer is deposited incrementally, minimizing interfacial disturbance. This, in turn, leads to a more controllable and stable initial interface between melt layers.

2. Experimental method

2.1. System construction and operation

A brief description of the experimental apparatus has appeared previously [10]. Here we will describe the system and its operation in greater detail including the more recent modifications. The system shown in Fig.

0022-2461/89 $03.00 + .12

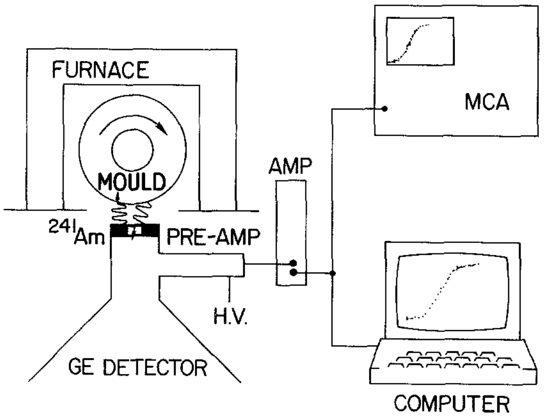

Figure 1 Experimental system.

1 basically enables the real-time, *in situ* monitoring of the composition of the liquid metal at the outer diameter of the rotating melt tube. This was accomplished through the generation of fluorescent X-rays from the melt employing a 30 mCi^{241} Am excitation source. The 60 keV gamma radiation from the latter passed through the heated (rotating) graphite mould wall. In turn, the backscattered melt-metal fluorescent X-rays traversed the mould wall and were detected and counted by a cryogenically cooled germanium detector. The latter was protected by a water-cooled radiation shield and located as close to the mould as possible to enable efficient counting. The associated counting electronics is similar to that employed in conventional X-ray energy-dispersive analysis systems. The amplified pulses were sent to a single-channel analyser for careful discrimination and then stored. A multichannel analyser (MCA) was sometimes used for this purpose. When operated in the time mode, the MCA has the useful feature of displaying the concentration build-up in time on a oscilloscope screen. Normally, however, the counts were stored in an Apple IIe microcomputer equipped with data acquisition hardware and software. The resultant count against time data were then transmitted to a VAX 11/780 computer where regression analysis diffusion coefficient determinations were performed.

The graphite mould containing the molten diffusion couple was machined from high-density graphite and contained a cylindrical cavity 5 cm long and 5 cm in diameter as shown in Fig. 2. The mould wall thickness was a compromise between the conflicting demands of high X-ray transmission and strength to withstand the centrifugally induced hoop stresses. To strengthen the outer mould surface, 1 cm thick ribs were machined into it, and these surrounded regions with a wall thickness of about 0.5 cm in a picture-frame pattern. The sealed end of the mould was screwed into a steel receptacle connected to a rotor shaft driven by a variable-speed, one-half horsepower direct-current motor. An intermediate set of radial bearings within pillow blocks served to thermally isolate the furnace-mould assembly from the motor shaft. A nichrome wire-wound furnace, whose temperature was maintained by an LFE programmable controller, surrounded the mould on three sides. The open side was exposed to the radioactive source-detector assembly. With such an arrangement the maximum operating temperature of the centrifuge was 550° C.

By virtue of the high rotational speed, it is unlikely that there were any circumferential temperature gradients within the mould. In order to investigate the magnitude of the longitudinal temperature gradient, fine thermocouples were positioned at the front, middle and back of the mould with the hot junctions cemented to the graphite and buried within the melt. The thermocouple wires were connected to the contacts of a precision slip ring, capable of maintaining electrical continuity at 5000 r.p.m., which was attached to the rotating shaft. The temperatures were calibrated against known melting points. Measured longitudinal temperature gradients over a 5 cm length were found to be no greater than 2.5° C during cooling of the metal and less than 1° C during the isothermal diffusion anneals.

The molten metal was poured into the horizontally rotating mould using either a curved graphite-coated spout or a narrow cylindrical graphite crucible. In the latter case the crucible was inserted into the mouth of the mould and positioned coaxially with respect to the axis of rotation. The metal was then melted *in situ*. At the appropriate moment this crucible was rotated through 180°, releasing its contents through a wide pouring slit in a sheet-like stream on to the prior-rotating melt.

2.2. Composition monitoring

The selection of experimental systems to be studied

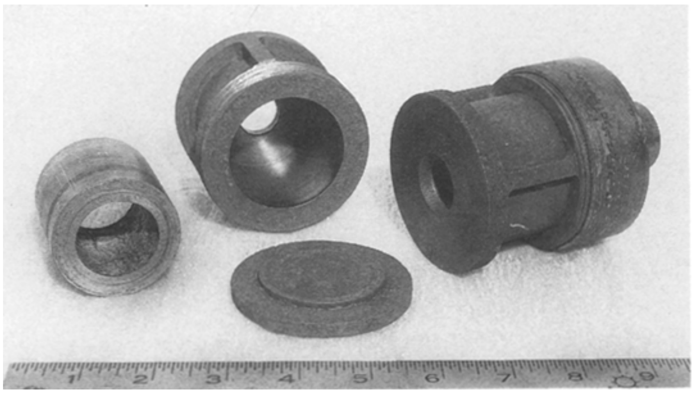

Figure 2 Graphite mould assembly together with a centrifugally cast composite Bi–Sn tube.

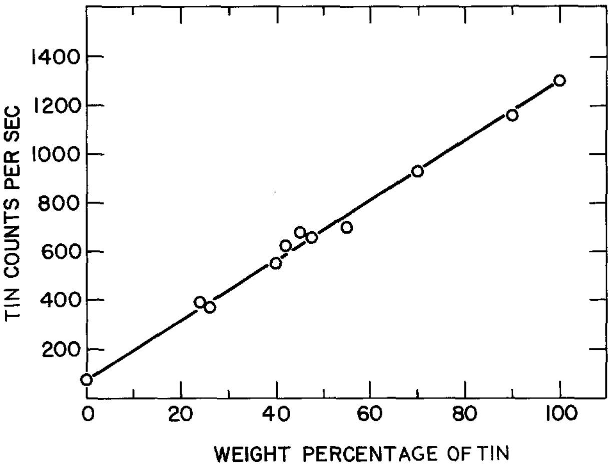

Figure 3 Calibration plot of tin count rate (per sec) against tin concentration in standard Sn–Zn alloys.

was influenced by the ease of separating and counting characteristic K and L X-ray lines. Through trial-and-error experimentation on the excitation of candidate metals situated behind a graphite absorber, it was found that fluorescent X-rays with energies greater than approximately 20 keV were suitable for counting. This, coupled with the temperature constraint, limited the choice of alloys to those containing tin, indium or cadmium. The K X-rays for these metals fall in the range 23 to 26 keV. Other low-melting elements such as lead and bismuth or gallium and zinc yield L or K X-rays, respectively, in the range 8 to 12 keV. Unfortunately X-rays with these energies proved difficult to count because they were less efficiently excited by the 60 keV source radiation and less readily counted by the germanium detector. Most importantly, they were more efficiently scattered by graphite so that the elemental signal-to-background noise was inadequate for measurement. Therefore, the concentration–time curves were deduced from the K X-ray yields of tin, indium and cadmium where typical count rates of 1000 to 1500 per second were measured in pure melts of these metals. Under these conditions the elemental peak count rate to background ratio was between 15 : 1 and 20 : 1.

In order to extract diffusivity values the raw X-ray count data had to be converted into actual compositions. For this purpose a set of alloy composition standards was established in each of the systems studied. Most of the standards utilized took the form of thin, rapidly cooled, cast plates which were positioned behind graphite absorbers of appropriate thickness during measurements. A direct calibration of composition against X-ray yield was then determined. Alternately, calibrations were made directly by measuring the X-ray yield from rotating melts of known homogeneous composition. Such a calibration for the Sn–Zn system is shown in Fig. 3 where, fortunately, the linear behaviour enabled a direct conversion to concentration without further correction. The situation was more complicated however in other alloy systems, e.g. Bi–Sn, Pb–Sn and Bi–In, where non-linear behaviour was obtained. In Bi–Sn, for example, the raw data are shown in Fig. 4a. Fortuitously, however, it was found that a plot of count rates against $C_iM_i/(C_1M_1 + C_2M_2)$ was remarkable linear as shown in Fig. 4b. The quantities C_i and M_i ($i = 1, 2$) refer to the weight percentages and atomic weights, respectively, of the components involved. This calibration procedure was also found to work well for the Pb–Sn and Bi–In systems and was utilized in the data analysis of these systems.

3. Results

Three pieces of sample data will be presented in order to illustrate various capabilities and features of the system in diffusion studies. In Fig. 5 data in the Bi–Sn system are shown at 300° C for the composition range 0 to 16 at % Sn. The results are clearly suggestive of a diffusive build-up, with a characterisitic incubation period, followed by a more rapid increase in concentration, ending with a slow approach to the steady-state concentration. Although the counting time exceeded 17 000 sec in this example, times ranging from 4000 to 30 000 sec were necessary in other systems depending on the couple geometry and diffusivities involved.

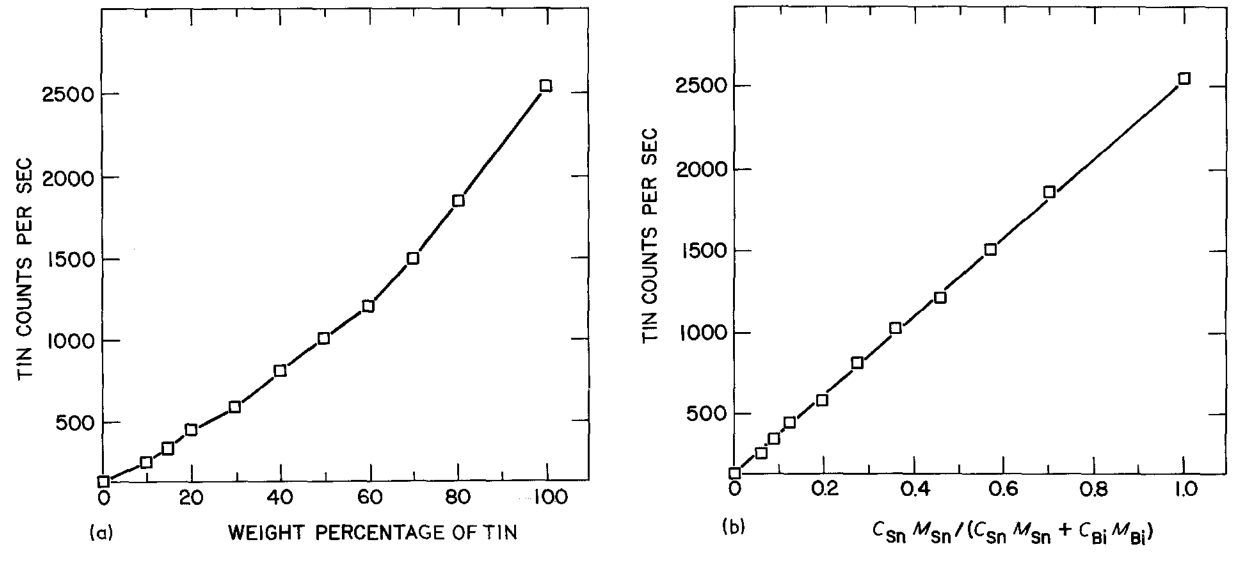

Figure 4 (a) Calibration plot of tin count rate (per sec) against tin concentration in standard Bi–Sn alloys. (b) Linear calibration plot of tin count rate (per sec) against $C_{Sn}M_{Sn}/(C_{Sn}M_{Sn} + C_{Bi}M_{Bi})$.

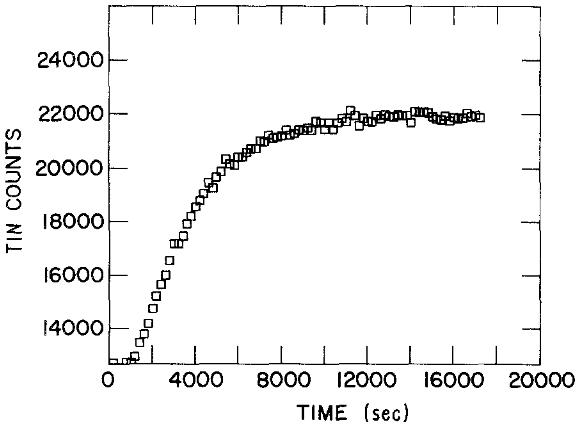

Figure 5 Tin counts against time for interdiffusion in a Bi–Sn couple, over the concentration range 0 to 16 at % Sn, at 300° C. (Counting time is 20 sec per point.)

The sensitivity of the technique is illustrated in Fig. 6, showing the interdiffusion kinetics over a total composition range of 1.3 wt % Sn in a Bi–Sn alloy.

Lastly, some data in the Sn–Zn system are shown in Fig. 7 where the composition range 30 to 78 wt % was spanned at 450° C. The anomalous feature of apparently linear kinetics ending abruptly at the steady-state count level is clearly different from the diffusional concentration build-up shown in Figs 5 and 6. This anomalous behaviour only occurred when the inner layer was pure zinc and provided the only exception to "normal" kinetics observed in the systems studied. An attempt to extract a diffusion coefficient from the anomalous kinetics by the procedure described in the next section resulted in an apparent value which was an order of magnitude larger than expected. The cause of this behaviour as well as its significance with regard to diffusion measurements will be discussed subsequently.

4. Data analysis and interpretation

4.1. Diffusion

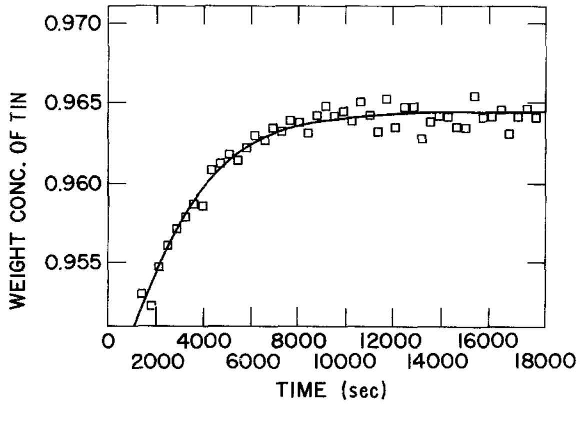

Figure 6 Interdiffusion kinetics in a Bi–Sn couple, over the range 0.95 to 0.963 weight fraction of tin, at 300° C.

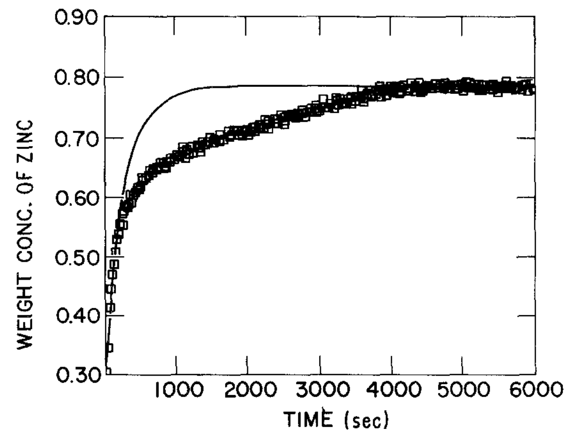

Figure 7 Anomalous interdiffusion kinetics in the Sn–Zn system, over the weight concentration range 0.30 to 0.78, at 450° C.

In order to extract the diffusion coefficient D from interdiffusion data shown typically in Fig. 5, the non-steady-state diffusion equation had to be solved subject to the initial and boundary conditions. The effect of the centrifugal field on atomic separation and diffusion is negligible at 100 *g* and not included in the diffusion equation. For the cylindrical geometry, where C, r and t are concentration, radial dimension and time, respectively, and D is assumed to be constant, the following hold:

$$\frac{\partial C(r,t)}{\partial t} = \frac{D}{r}\frac{\partial}{\partial r}\left| r\frac{\partial C(r,t)}{\partial r} \right| \qquad (1)$$

$$\frac{\partial C}{\partial r} = 0 \quad \text{at } r = r_o \text{ (the outer radius)} \qquad (2a)$$

$$\frac{\partial C}{\partial r} = 0 \quad \text{at } r = r_i \text{ (the inner radius)} \qquad (2b)$$

The latter conditions express the fact that no mass can flow across these two surfaces.

Initially (at $t = 0$)

$$C = C_1 \quad \text{for } r_i < r < r_m \qquad (3a)$$

and

$$C = C_2 \quad \text{for } r_m < r < r_o \qquad (3b)$$

The layer thicknesses are a and b, defined by $a = r_m - r_i$ and $b = r_o - r_m$ where r_m is the radius at the initial couple interface. The general solution for $C(r, t)$ is given, after separation of variables, by

$$C(r,t) = \sum_{n=0}^{\infty} a_n(0)\, e^{-K_n^2 Dt}\, \phi_n(r) \qquad (4)$$

where ϕ_n satisfies

$$\frac{d^2\phi_n}{dr^2} + \frac{1}{r}\frac{d\phi_n}{dr} + K_n^2\phi_n = 0 \qquad (5)$$

ϕ_n, in turn, is given by a linear combination of Bessel

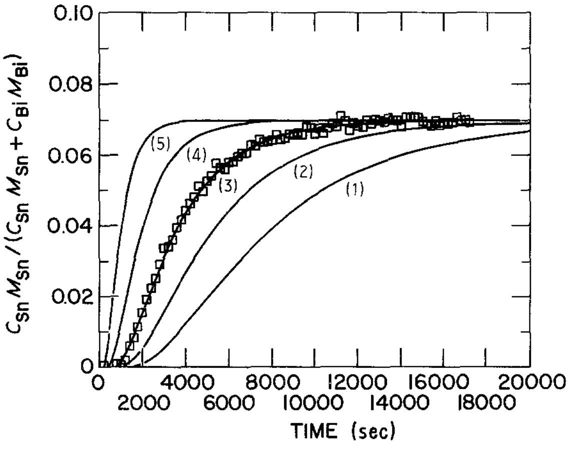

Figure 8 Computer fits to Bi–Sn interdiffusion data. Effective tin concentration against time; D values ($cm^2\,sec^{-1}$) are (1) 10^{-5}, (2) 1.5×10^{-5}, (3) 2.35×10^{-5}, (4) 4.0×10^{-5}, (5) 8×10^{-5}.

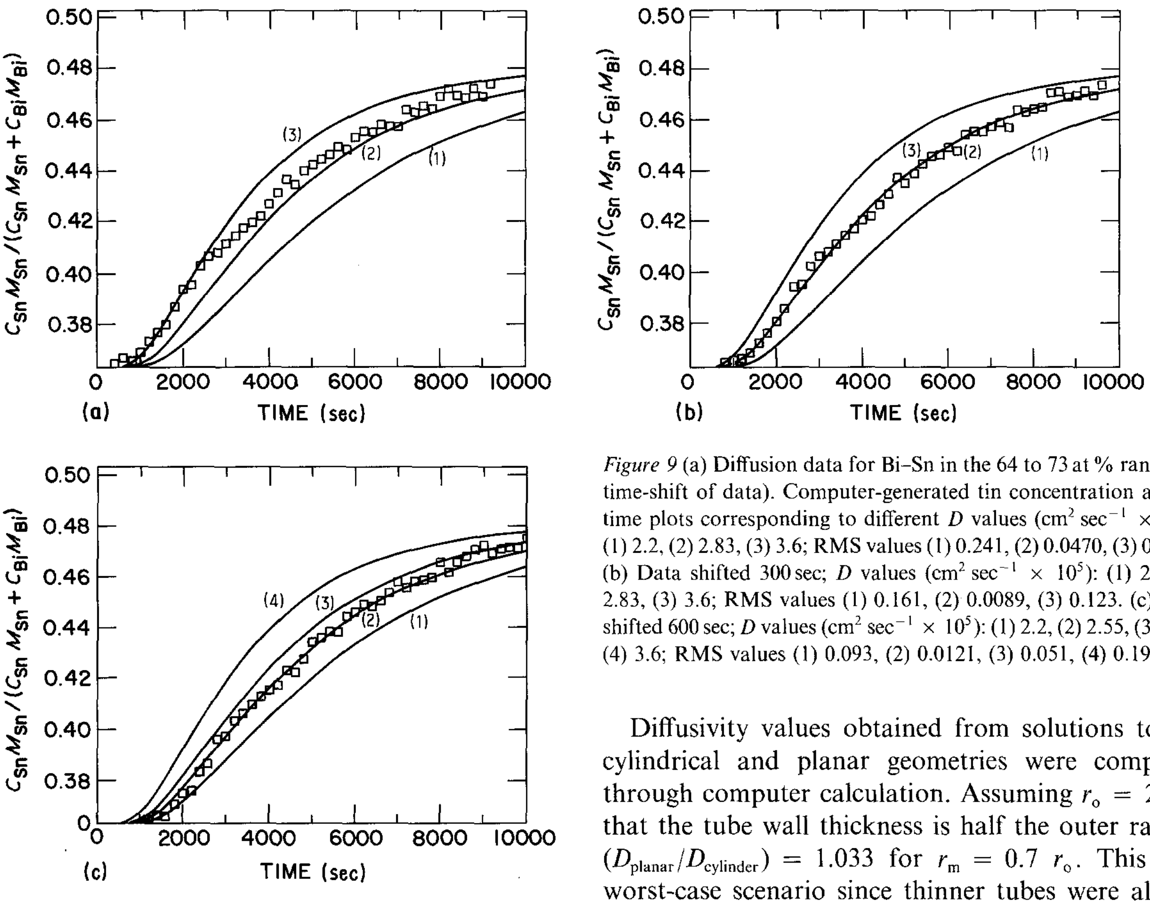

Figure 9 (a) Diffusion data for Bi–Sn in the 64 to 73 at % range (no time-shift of data). Computer-generated tin concentration against time plots corresponding to different D values ($\text{cm}^2\,\text{sec}^{-1} \times 10^5$): (1) 2.2, (2) 2.83, (3) 3.6; RMS values (1) 0.241, (2) 0.0470, (3) 0.0431. (b) Data shifted 300 sec; D values ($\text{cm}^2\,\text{sec}^{-1} \times 10^5$): (1) 2.2, (2) 2.83, (3) 3.6; RMS values (1) 0.161, (2) 0.0089, (3) 0.123. (c) Data shifted 600 sec; D values ($\text{cm}^2\,\text{sec}^{-1} \times 10^5$): (1) 2.2, (2) 2.55, (3) 2.83, (4) 3.6; RMS values (1) 0.093, (2) 0.0121, (3) 0.051, (4) 0.196.

(J_0) and Neumann (N_0) functions as

$$\phi_n(r) = A_n J_0(K_n r) + B_n N_0(K_n r) \qquad (6)$$

where A_n and B_n are constants. The two boundary conditions enable the eigenvalues, K_n, to be determined from the condition that

$$\text{Det} \begin{vmatrix} J_0'(K_n r_i) & N_0'(K_n r_i) \\ J_0'(K_n r_o) & N_0'(K_n r_o) \end{vmatrix} = 0 \qquad (7)$$

Lastly $a_n(0)$ is given by

$$a_n(0) = C_1 \int_{r_i}^{r_m} r\phi_n(r)\,\mathrm{d}r + C_2 \int_{r_m}^{r_o} r\phi_n(r)\,\mathrm{d}r \qquad (8)$$

The measured concentration corresponds to $C(r, t)$ evaluted at $r = r_o$.

The solution of the non-steady-state diffusion equation is very much simplified if the curved bilayer configuration is replaced by a linear diffusion couple. In this case

$$\frac{\partial C(x, t)}{\partial t} = D \frac{\partial^2 C(x, t)}{\partial x^2} \qquad (9)$$

and $(\partial C/\partial x) = 0$ at $x = 0$ and at $x = a + b$, the two bounding surfaces. The initial condition is that $C = C_1$ for $0 < x < a$ and $C = C_2$ for $a < x < b$. The solution for the concentration build-up at $x = a + b$, the surface being probed, is given by

$$C(x = a + b, t) = \frac{C_1 a + C_2 b}{a + b} + \frac{2(C_1 - C_2)}{\pi} \times \sum_{n=1}^{\infty} \frac{(-1)^n}{n} \sin \frac{n\pi a}{a + b}\, \mathrm{e}^{-n^2\pi^2 Dt/(a+b)^2} \qquad (10)$$

Diffusivity values obtained from solutions to the cylindrical and planar geometries were compared through computer calculation. Assuming $r_o = 2r_i$ so that the tube wall thickness is half the outer radius, $(D_{\text{planar}}/D_{\text{cylinder}}) = 1.033$ for $r_m = 0.7\ r_o$. This is a worst-case scenario since thinner tubes were always poured. When the tube thickness is $0.2r_o$, a more representative value, the two diffusivities differ by only 0.35%. The error in D obtained by fitting data to Equation 10 rather than Equation 4 is, therefore, estimated to be considerably less than that arising from experimental measurement uncertainties.

The procedure for determining the diffusion coefficients was therefore the following:

1. Experimental count-against time data were generated as shown typically in Fig. 5.
2. Theoretical curves, representing solutions to Equation 10 for several candidate D values, were plotted. The vertical axis was simply the appropriate concentration given by the calibration. The calculated results were superimposed over the experimental data as shown in Fig. 8.
3. The curve that results in the lowest root mean square (RMS) of residuals corresponds to the statistically best values of the diffusion coefficient.

In the course of the analysis of diffusion data, it was observed that some of the experimental diffusion curves had to be horizontally shifted in order to ensure the lowest RMS of residuals. In other words, the incubation period (the time at which a concentration build-up is first recorded for a given diffusion run within the sensitivity limits of the system) was shorter than for the corresponding theoretically derived time. The diffusion curve requiring a time shift of 300 sec, the largest encountered in this work, is shown in Fig. 9a. None of the theoretical curves on the plot follows the data tendency except perhaps the curve for $D = 2.83 \times 10^{-5}\,\text{cm}^2\,\text{sec}^{-1}$, but the curve clearly does not model the data accurately. Fig. 9b shows the same theoretical and experimental curves after the

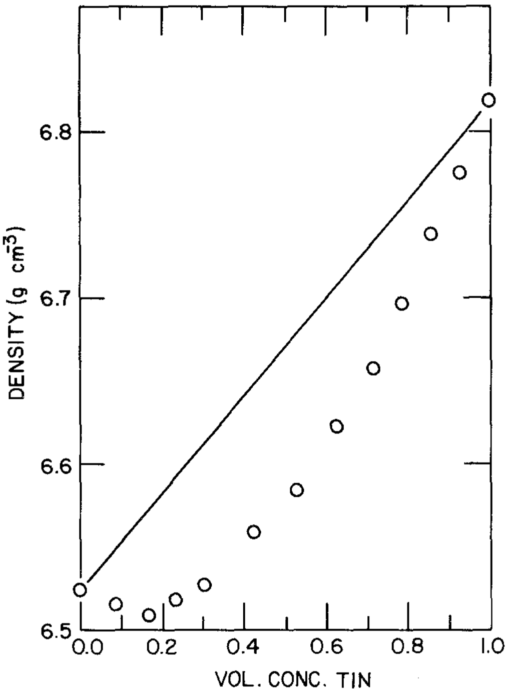

Figure 10 Density of Sn–Zn alloys against volume concentration of tin at 450° C.

experimental data were translated for 300 sec along the time axis. The $D = 2.83 \times 10^{-5}$ cm^2 sec^{-1} curve now fits the data and has an RMS of residuals value as low as 0.0089 (lower than for the original case by a factor of four). Fig. 9c indicates that a parallel translation of the data by 600 sec again results in a significantly higher RMS of residuals.

Attaining the best statistical fit of the experimental data to the theoretical model is the practical justification for the appropriate horizontal shift of the data. From a phenomenological standpoint, the lower incubation time can be explained in terms of the initial disturbance at the interface between the two liquid layers due to the impingement of the incoming second layer on to the surface of the first (outer) liquid layer. As the bilayer melt configuration during the diffusion experiments is stable, the disturbance is damped. The decay of the disturbance, whether aperiodic (rapid viscous or slow creeping) or oscillatory, still takes a finite time during which complex blending at the interface may occur. This alters the initial boundary condition assumed in the solution to the non-steady-state diffusion equation. This change in the initial condition will have an effect on the incubation time, but will have a much lesser influence on the subsequent long-time kinetics of the solute build-up. Therefore, the simple horizontal translation of the diffusion curve was performed during the data analyses in several instances.

4.2. Anomalous transport

The apparent non-diffusion kinetics of Fig. 7 can be explained by referring to Fig. 10 which depicts the density of Sn–Zn melts at 450° C as a function of concentration. The densities were calculated using the volume-of-mixing data reported by Kleppa *et al.* [11]. Due to the closeness in the densities of tin and zinc, upon mixing the curve actually exhibits a minimum at about 16 vol % Sn (10 at % Sn). Pure zinc appears to have a higher density than Sn–Zn alloys with up to 18 at % Sn. The volume-of-mixing data were indirectly verified by conducting a centrifugation experiment which involved pouring a layer of pure zinc on to a molten layer of rotating 7 at % Sn–Zn alloy. The resulting rapid intermixing kinetics (shown in Fig. 11) clearly indicates that mass transport was controlled by the development of a Rayleigh–Taylor instability [12]. Thus the anomalous transport of Fig. 7 is the result of the formation of Sn–Zn alloy melts which are less dense than the pure zinc layer at the inner diameter. A Rayleigh–Taylor instability developed and resulted in non-diffusive transport kinetics. Only when the tin concentration at the outer diameter exceeded 18 at % did the bilayer configuration become stable from the standpoint of fluid dynamics. Subsequently, interdiffusion occurred with a kinetics dependent on the complex composition distribution through the melt created by the prior instability transport. It must be emphasized that the non-diffusive character of the mass transport was recognized during the real-time evolution of the shape of the concentration kinetics curve. This is an advantage since other techniques involving "post-mortem" determination of the solute distribution in solidified metals would simply suggest an exceedingly large diffusivity value.

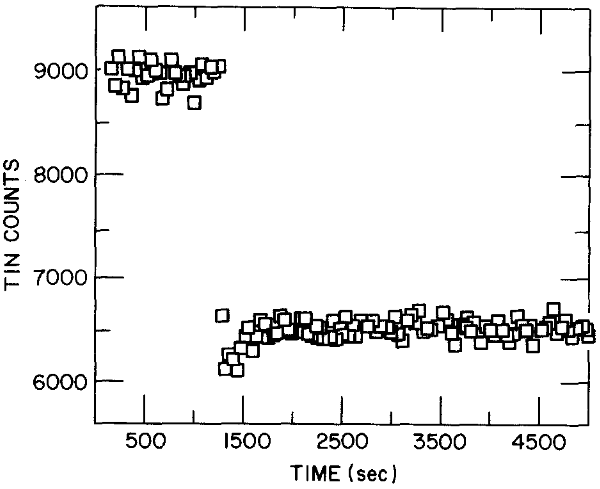

Figure 11 Tin counts against time for a mechanically unstable bilayer melt. Density difference between pure zinc and 7 at % Sn–Zn is one part in 650.

5. Conclusions

1. A new real-time experimental technique was developed having general applicability to the study of a variety of mass transport phenomena in liquid alloys. The applications of this technique to diffusion studies have been described.

2. Unlike traditional techniques, the determination of diffusion coefficients is based on the *in situ* analysis of molten alloys. The uncertainties associated with solute redistribution during solidification are therefore eliminated.

3. The diffusion coefficients are determined based on the kinetics of solute build-up. Non-diffusive contributions to the mass transport can therefore be detected from anomalies in the shape of the curve.

Acknowledgements

We are grateful to the Abex Corporation of Mahwah, New Jersey for their support of and interest in this work. The authors benefited from many discussions with Professor Harold Salwen and sincerely thank him for his many contributions to this work. The technical assistance provided by Mr R. Bayer is very much appreciated. Lastly, for many reasons, we dedicate this work to the memory of Dr Hugo Larson.

References

1. N. H. NACHTRIEB, in "Properties of Liquid Metals", edited by P. D. Adams (Taylor & Francis, London, 1976) p. 309.
2. J. B. EDWARDS, E. E. HUCKE and J. J. MARTIN, *Metal Rev.* **13** (1968) 1.
3. H. A. WALLS, in "Physiochemical Measurements in Metals Research", Vol. 4, Part 2, edited by R. A. Rapp (Wiley, New York, 1970) p. 459.
4. N. H. NACHTRIEB, in "The Properties of Liquid Metals", edited by S. Takeuchi (Taylor & Francis, London, 1973) p. 521.
5. *Idem*, in "Liquid Metals", edited by S. Z. Beer (Dekker, New York, 1972) p. 518.
6. D. A. RIGNEY, in Institute of Physics Conference Series No. 30 (Institute of Physics, London, 1977) p. 619.
7. M. SHIMOJI and T. ITAMI, "Diffusion and Defect Data", Vol. 43 (1986) p. 154.
8. A. Z. BROUCKA, J. O'M. BOCKRIS and J. J. KITCHENER, *Proc. R. Soc.* **A241** (1957) 554.
9. D. K. BELASCHENKO, *Russ. J. Phys. Chem.* **39** (1965) 711.
10. I. KHANDROS and M. OHRING, *Scripta Metall.* **18** (1984) 1355.
11. O. J. KLEPPA, M. KAPLAN and C. E. THALMAYER, *J. Phys. Chem.* **65** (1961) 843.
12. I. Y. KHANDROS, PhD thesis, Stevens Institute of Technology (1985) p. 65.

Received 15 December 1987
and accepted 6 May 1988